CHEMISTRY OF MATERIALS

ARTICLE

pubs.acs.org/cm

Phase Stability and Permeation Behavior of a Dead-End $Ba_{0.5}Sr_{0.5}Co_{0.8}Fe_{0.2}O_{3-\delta}$ Tube Membrane in High-Purity Oxygen Production

Fangyi Liang,[†] Heqing Jiang,[‡] Huixia Luo,[†] Jürgen Caro,[†] and Armin Feldhoff*[,†]

[†]Institute of Physical Chemistry and Electrochemistry, Leibniz University Hannover, Callinstrasse 3A, D-30167 Hannover, Germany

[‡]Max-Planck-Institut für Kohlenforschung, Kaiser-Wilhelm-Platz 1 D-45470 Mülheim an der Ruhr, Germany

ABSTRACT: Phase stability and oxygen permeation behavior of $Ba_{0.5}Sr_{0.5}Co_{0.8}Fe_{0.2}O_{3-\delta}$ (BSCF) dead-end tube membranes were investigated in long-term oxygen production at 950 and 750 °C. At 950 °C, the BSCF tube membranes exhibit good long-term phase stability and a stable oxygen permeation flux. However, at the intermediate temperature of 750 °C, both the oxygen permeation flux and the oxygen purity decrease continuously. This behavior is related to the formation of two secondary phases that are a hexagonal perovskite, $Ba_{0.5\pm x}Sr_{0.5\pm x}CoO_{3-\delta}$, and a trigonal mixed oxide, $Ba_{1-x}Sr_xCo_{2-y}Fe_yO_5$, that evolved in the ceramic membrane made of cubic BSCF perovskite during the dynamic flow of oxygen through it. Tensile stress as a result of phase formation causes the development of cracks in the membrane, which spoil the purity of the permeated oxygen. The partial degradation of cubic BSCF perovskite in the intermediate temperature range (750 °C) was more pronounced under the strongly oxidizing conditions on the oxygen supply (feed) side than on the oxygen release (permeate) side of the membrane. The structural instability of BSCF is attributed to an unsuitable redox state of cobalt, that exhibits an ionic radius that is too small to be tolerated by the cubic perovskite structure, which then becomes unstable. The phase stability of cubic BSCF (i.e., the proper redox states of cobalt) can be maintained by operating the membrane in the high temperature regime (950 °C).

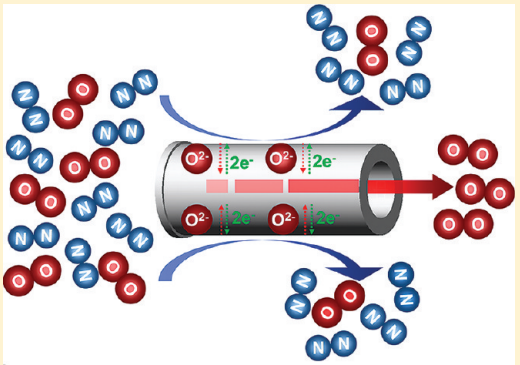

KEYWORDS: perovskite, mixed conductor, decomposition, oxygen permeation, oxygen production

1. INTRODUCTION

Oxygen is the third-largest-volume chemical produced worldwide,[1] and most of the industrial applications for oxygen require high-purity oxygen. Oxygen-transporting membranes (OTMs) can separate oxygen from air, which is a gas mixture containing approximately 78 vol % N_2 and 21 vol % O_2,[2] or from other oxygen-containing gases. OTMs can theoretically produce oxygen at purities of up to 100% and are believed to possess the potential to reduce the cost of high-purity oxygen production compared to the conventional cryogenic processes.[3] Moreover, OTM reactors have been developed for such potential applications as the partial oxidation of hydrocarbons,[4−8] the production of hydrogen by thermal water splitting in combination with olefin and synthesis gas production,[9−11] and the decomposition of nitrogen oxides.[12,13]

High-purity oxygen can be obtained with the use of OTMs when the oxygen partial pressure at one surface (feed side) is higher than that at the opposite surface (permeate side). The oxygen partial pressure difference can be achieved through the elevation of the oxygen partial pressure on the feed side by the compression of air to pressures higher than 1 bar, the reduction of the oxygen pressure on the permeate side by a vacuum pump, a combination of both techniques, or the use of steam as a condensable sweep gas on the permeate side.[14] The thermal activation of a membrane's oxygen-transport properties requires the OTM to operate at temperatures of approximately 700−950 °C. The authors of several studies on the high-purity oxygen production have been reported using tubular membrane geometries, instead of conventional flat disks, which are capillary hollow-fiber[15,16] or tube membranes[17,18] that overcome the problem of high-temperature sealing by allowing the seal to be placed in the cold zone.

In the past few decades, many OTMs with high oxygen permeabilities have been developed that are based on mixed ionic-electronic conductors (MIEC) solid oxides, such as $SrCo_{0.8}Fe_{0.2}O_{3-\delta}$,[19] $BaCo_{0.4}Fe_{0.4}Zr_{0.2}O_{3-\delta}$,[20] $BaCo_{0.7}Fe_{0.2}Ta_{0.1}O_{3-\delta}$,[21] $Ba_{0.5}Sr_{0.5}Fe_{0.9}Al_{0.1}O_{3-\delta}$,[22] $Ba_{0.5}Sr_{0.5}Fe_{0.8}Cu_{0.2}O_{3-\delta}$,[23] and $Ba_{0.5}Sr_{0.5}Co_{0.8}Fe_{0.2}O_{3-\delta}$ (denoted BSCF).[24] Among these compounds, BSCF, which assumes a cubic perovskite structure, has been regarded as one of the most promising materials for oxygen separation from air and for cathodes in solid-oxide fuel cells.[25] Because of the high concentration of the mobile oxygen vacancies in the perovskite lattice,[26] BSCF exhibits a very high oxygen-permeation flux over a wide temperature range.[24] Zhu et al.[18] have observed the stable oxygen permeation behavior of a BSCF perovskite tube membrane under vacuum and elevated pressures

Received: June 24, 2011
Revised: September 20, 2011
Published: October 07, 2011

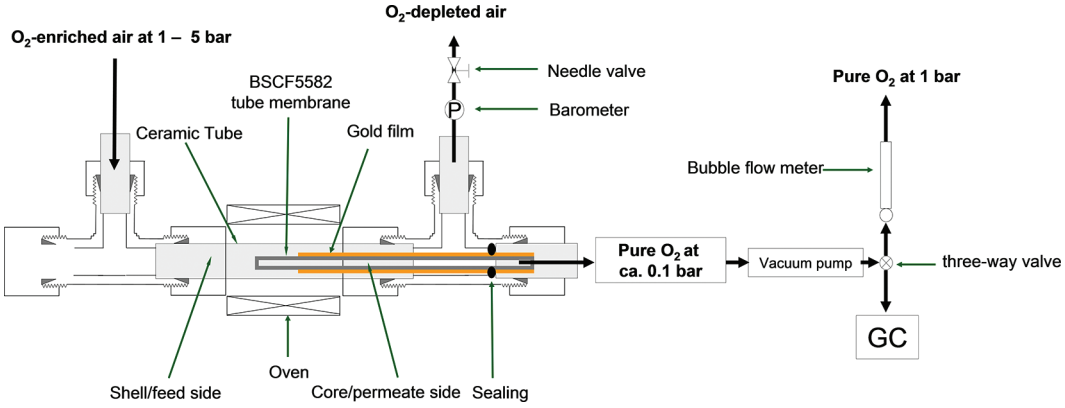

Figure 1. Permeator in dead-end geometry for the production of high-purity oxygen.

for high-purity oxygen production at 925 °C. However, Shao et al.[24] and van Veen et al.[27] have reported that stable oxygen permeation is achieved only when the operating temperatures are higher than 850 °C. During operation in the intermediate temperature (IT, i.e., approximately 500−850 °C) range, however, the oxygen-permeation flux through the BSCF membrane has been observed to decrease, which has been attributed in several reports[24,28−31] to a partial decomposition of the bulk cubic perovskite phase. Shao et al.[24] and Rebeilleau-Dassoneville et al.[28] have observed reflections of noncubic phases in the X-ray diffraction (XRD) patterns of BSCF after the samples were annealed in the IT range. Based on the same experimental technique, Švarcová et al.[30] have described the occurrence of hexagonal perovskite (2H or 4H polymorphs) in addition to the cubic phase. Arnold et al.[29,32] have investigated the formation of cubic BSCF in a sol−gel-based process by analyzing XRD powder patterns that were obtained in situ in the IT range and from quenched intermediate powders. They observed diffraction patterns similar to those observed by Švarcová et al.[30] during partial decomposition of BSCF in the same temperature range. They also noted the reciprocity between the formation and decomposition processes of BSCF. Using transmission electron microscopy (TEM), Arnold et al.[29] clearly showed that some phases, that evolved in the IT range can be described as distorted polytypes with different sequences of cubic and hexagonal close-packed layers, that consist of oxygen and A-site cations (Ba or Sr). These polytypes therefore constitute intergrown structures of cubic and 2H hexagonal perovskite. Using TEM, Mueller et al.[33] observed structural changes not only in the grain boundaries of polycrystalline BSCF ceramic, but also in the BSCF grains themselves by the formation of extended platelets. They mainly addressed the grain boundaries and found barium and cobalt-enriched 2H hexagonal perovskite. Efimov et al.[31] studied, by TEM, BSCF powder and ceramic that had been exposed to IT. They found not only barium- and cobalt-enriched hexagonal perovskite, which was assigned an approximate stoichiometry of $Ba_{0.6}Sr_{0.4}CoO_{3-\delta}$, but also barium-enriched and heavily cobalt-enriched trigonal 15R-related $Ba_{1-x}Sr_xCo_{2-y}Fe_yO_{5-\delta}$. The first XRD diffractograms taken by Shao et al.[24] of a BSCF membrane after it was dynamically operated in an oxygen permeation flux for 400 h at 750 °C showed significantly stronger reflection intensities from additional phases on the feed (air) side as compared to the permeate (helium) side. Microstructure investigations in the aforementioned studies, however, were made solely on BSCF powders or ceramic pellets after they were annealed in a static (air) atmosphere.

In this report, we extend the work of Shao et al.[24] and investigate the microstructure of a BSCF membrane, which developed during operation under a dynamic flow of oxygen in the IT range, by scanning electron microscopy (SEM) analysis, TEM, and XRD. We correlate the observed membrane microstructure, which differs between the feed and permeate side, with the oxygen permeation behavior (i.e., oxygen flux and oxygen purity). Dead-end BSCF tube membranes were used for the high-purity oxygen production using air or oxygen-enriched air as feed gases.

2. EXPERIMENTAL SECTION

Oxygen Production in Dead-End Membrane Reactor. The $Ba_{0.5}Sr_{0.5}Co_{0.8}Fe_{0.2}O_{3-\delta}$ (BSCF) tubes (400 mm long, 10 mm outer diameter, 1 mm wall thickness) were purchased from Fraunhofer Institute IKTS Dresden/Hermsdorf (Germany). One of the two ends of the tube is closed by an approximately 1 mm thick disk of the same BSCF material.[34]

Oxygen was produced in a dead-end membrane permeator as shown in Figure 1. A stream of air, as a nitrogen/oxygen mixture, is supplied from the left to the dead end of the tube and leaves the setup as oxygen-depleted air. Oxygen permeates the MIEC tube walls via a flux of oxygen anions, which is accompanied by counterflowing electrons. Permeated oxygen leaves the setup to the right via the interior of the tube to the right. In the experiment, parts of the tube membrane were coated by a gold paste (Heraeus), except the 3 cm part near the dead end. The tube segment was painted by the Au paste, which then was sintered at 950 °C for 5 h. This procedure was applied 3-fold to obtain a dense gold film, which the oxygen can not permeate. Inspection by light microscope of the gold sealing after long-term permeation experiment revealed a still hole- and crack-free dense layer. This is consistent with the good compatibility of gold sealant with perovskite membrane as reported by Tong et al.[35] for 2000 h long high-temperature experiments. The uncoated part of our tube with an effective membrane area of 9.1 cm^2 for the outer membrane surface was placed in the middle of the oven, thus ensuring isothermal conditions. Oxygen-enriched air with 50 vol. % O_2 at an elevated pressure of 5 bar was fed at a rate of 500 cm^3(STP)min^{-1} to the feed side. Flow rates were controlled by gas mass-flow controllers (Bronkhorst). High-purity oxygen was produced at approximately 0.1 bar on the core/permeate side. This reduced pressure was achieved with a vacuum pump (Pfeiffer vacuum MVP 015−4). The flow of the outlet on the core/permeate side was mixed with neon (1.0 cm^3 (STP)min^{-1}, 99.995%) as an internal standardization gas, which allowed the determination of the absolute flux of the permeate gas by an online coupled gas chromatograph (Agilent 7890A) that was equipped with a Carboxen 1000 column.

dx.doi.org/10.1021/cm2018086 |*Chem. Mater.* 2011, 23, 4765–4772

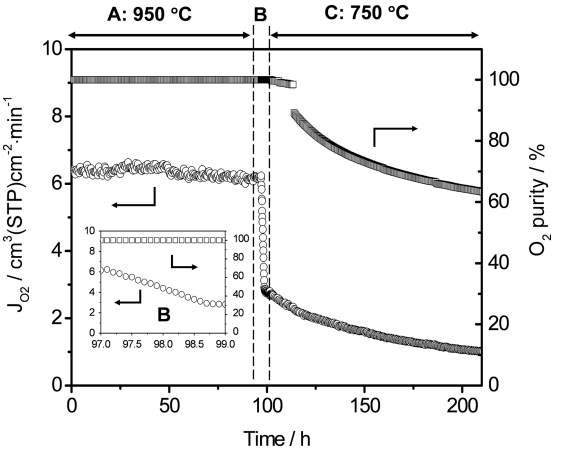

Figure 2. Long-term operation of oxygen production using a dead-end BSCF tube membrane at 950 and 750 °C. Shell/feed side: 50 vol % oxygen-enriched air at 5 bar with a flow rate of 500 cm^3(STP) min^{-1}. Core/permeate side: O_2 at approximately 0.1 bar. Inset B shows the continuous decrease of the oxygen flux from the isothermal region A at 950 °C to the isothermal region C at 750 °C. For the associated XRD results, see Figure 7; for SEM micrographs see Figure 8.

The leaking of nitrogen and oxygen through pores or cracks is assumed to be in accordance with the Knudsen diffusion mechanism. Then, for the experiment with 50 vol % oxygen-enriched air at the feed side, the fluxes of leaked nitrogen and oxygen are related by eq 1.

$$J_{N_2}^{Leak} : J_{O_2}^{Leak} = \sqrt{\frac{32}{28}}\frac{0.5}{0.5} = 1.07 \quad (1)$$

The oxygen permeation flux J_{O_2} (cm^3 (STP) min^{-1} cm^{-2}) can be calculated by eq 2, in which the leakage of oxygen is subtracted by taking into account the leakage of nitrogen.

$$J_{O_2} = \left(C_{O_2} - \frac{C_{N_2}}{1.07}\right)\frac{F}{S} \quad (2)$$

Here, C_{O_2} and C_{N_2} are the oxygen and nitrogen concentrations estimated from calibrated gas chromatograph. F is the total flow rate of the outlet on the core/permeate side, and S is the effective surface for permeation.

Tools for Microstructure Analysis. The XRD data were collected in a $\theta/2\theta$ geometry on a Bruker D8 Advance instrument equipped with a Cu K_α radiation at 40 kV and 40 mA. A receiving slit of 0.05 mm was used and data were collected in step-scan mode in the 2θ range of $20° < 2\theta < 80°$ at intervals of 0.02°. Scanning electron microscopy (SEM) was performed with a JEOL JSM-6700F at a low excitation voltage of 2 kV for imaging with secondary electrons and at 5 kV for backscattered-electron channelling contrast imaging. Specimens for the latter purpose were prepared using a Buehler VibroMet 2 vibratory polisher. Transmission electron microscopy (TEM) was performed on a JEOL JEM-2100F that was equipped with a Gatan Imaging Filter (GIF 2001) and an Oxford Instruments INCA TEM 200 light-element energy-dispersive X-ray (EDX) spectrometer. Scanning transmission electron microscopy (STEM) imaging was performed on appropriate bright- and dark-field detectors. TEM imaging, selected area electron diffraction (SAED), and electron energy-loss spectroscopy (EELS) were performed on the charge-coupled device (CCD) camera of the GIF.

3. RESULTS AND DISCUSSION

Permeation Behavior of Dead-End BSCF Tube Membrane. The reliability of the dead-end BSCF tube membrane in the production of oxygen was evaluated with a feed of 50 vol % oxygen-enriched air at 5 bar and a reduced pressure of approximately 0.1 bar on the permeate side at 950 and 750 °C, as shown in Figure 2. The oxygen-enriched air with different oxygen contents can be produced by using either the organic polymeric

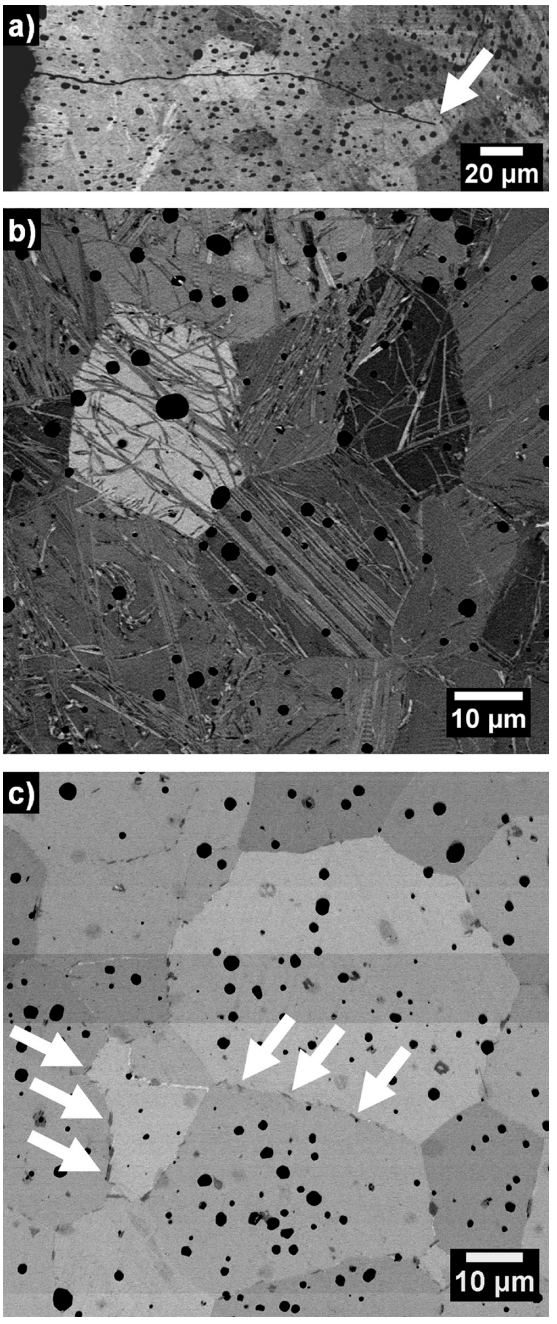

Figure 3. Backscattered-electron channelling contrast images of the BSCF perovskite tube membrane cross-section after the long-term permeation experiment shown in Figure 2 (100 h at 950 °C, 120 h at 750 °C): (a) Overview of shell/feed side showing an approximately 200 μm long crack running into the membrane from the left (shell/feed side). The crack tip is marked by an arrow. (b) Area close to the shell/feed side showing secondary phases criss-crossing BSCF grains. (c) Area close to core/permeate side showing secondary phases in the grain boundaries. Some phases are marked by arrows. Note that the closed porosity of the ceramic membrane appears as black dots.

dx.doi.org/10.1021/cm2018086 |Chem. Mater. 2011, 23, 4765–4772

hollow-fiber membranes[36] or perovskite hollow-fiber membranes.[15,37] At 950 °C, the oxygen-permeation flux and the oxygen purity were found to be constant over a time period of 100 h. A high oxygen purity of almost 100 vol % (gas chromatograph did not detect any N_2) and a stable oxygen permeation flux of 6.3 $cm^3cm^{-2}min^{-1}$ were observed. The high oxygen purity indicates that the gas leakage is negligible, even at a pressure difference of approximately 6 bar, because of the perfect connection between the BSCF tube and the BSCF disk that forms the dead-end part of the membrane. Moreover, the dead-end tube membrane's geometry can solve the problem of high-temperature sealing by allowing the use of silicon rings outside the high-temperature zone. A stable performance of a dead-end BSCF tube membrane with silver as sealant at 925 °C has also been reported by Zhu et al.[18]

When the temperature was slowly decreased by 2 $°Cmin^{-1}$ from 950 to 750 °C, the oxygen purity initially remains constant at 100%, but the oxygen-permeation flux continuously decreases from 6.6 to 2.8 cm^3 (STP) cm^{-2} min^{-1} (inset in Figure 2). At 750 °C, the oxygen-permeation flux decreases continuously with time from 2.8 cm^3 (STP) cm^{-2} min^{-1} to 1.0 $cm^3cm^{-2}min^{-1}$ after 120 h. This observation is in good agreement with the findings of Shao et al.,[24] van Veen at al.,[27] and Efimov et al.[31] At 750 °C, first the oxygen purity decreases slowly over 10 h. This initial decrease of in the oxygen concentration may be due to a low constant nitrogen flux that results from small sealing imperfections or membrane pin holes, which become increasingly significant if the oxygen flux is decreased by a decrease in the temperature. After approximately 10 h at 750 °C, a sudden decrease in the oxygen purity is observed which is related to the formation of small cracks in the membrane. The further growth of the cracks causes a further decrease of the oxygen purity with time, as shown in Figure 2. Cracks run radially from the perimeter (feed side) into the tube membrane and can be observed in SEM micrographs. After the permeation experiment shown in Figure 2 (100 h at 950 °C and 120 h at 750 °C) was completed, a cross-section of the tube membrane was prepared by vibration polishing to preserve the material's crystallinity to the very surface of the specimen so that backscattered-electron channelling contrast imaging could be applied. Figure 3a shows an overview of the shell/feed side with a crack approximately 200 μm in length. The crack appears black in contrast, because no material is present in the crack opening that could scatter the electrons to the detector. The same holds true for closed porosity, which also is seen as black.

Microstructure Overview. At the higher magnification in Figure 3b, orientation-dependent backscattered-electron channelling contrast allows not only individual BSCF grains with sizes of approximately 20−40 μm to be distinguished but also secondary phases in the grain boundaries and, more significantly, those running through the bulk grains. These secondary phases are predominantly observed in a region up to approximately 200 μm below the shell/feed side, which constitutes the side with the highest oxygen chemical potential in the permeation experiment. Remember, cracks are observed in the same region. Obviously, the formation of secondary phases leads to an accumulation of internal stresses. At the core/permeate side, which is shown in Figure 3c, the situation is different. Here, microstructure changes are essentially restricted to the grain boundaries that are decorated by platelike crystals. Almost no secondary phases run through the BSCF grains.

Microstructure at the Core/Permeate Side. The situation at the core/permeate side is shown in more detail in Figure 4a by bright-field TEM. The distribution of secondary phases at the boundary between BSCF grains 1 and 2 (**A** and **B**) is sketched in the STEM micrograph of Figure 4b. Based on the elemental distributions of Figures 4c to g, phase **B** is enriched in oxygen and in cobalt but depleted in strontium, as compared to BSCF. By quantification of the local EDX spectra, a 2:1 ratio of B-site to A-site cations was observed. This ratio is consistent with a com plex trigonal oxide of approximate composition $Ba_{1-x}Sr_xCo_{2-y}Fe_yO_{5-\delta}$, as reported by Efimov et al.[31] The compositional parameters of approximately $x = 0.15$ and $y = 0.25$, however, vary locally. In the **A** regions, smaller crystallites with diameters less than 200 nm were formed. These crystallites decorate the interface between the platelet of phase **B** and grain 1, but are also observed to the lower right. Their occurrence correlates with **A** regions that are almost free of iron (see Figure 4g). The quantification results of local EDX spectra show less than 1 at % iron. Enrichments of cobalt (Figure 4f) and oxygen (Figure 4c) are observed. It is noteworthy that barium and strontium content varies locally in the opposite manner (compare Figures 4d and e). With reference to Efimov et al.[31] and Mueller et al.,[33] we postulate that hexagonal perovskites $Ba_{0.5\pm x}Sr_{0.5\pm x}CoO_{3-\delta}$ (with $x \approx 0.1$) were formed in region **A**. Although a strontium-enriched hexagonal perovskite is not expected according to other investigators, Figures 4d, e, and g clearly indicate that iron depleted regions correlate with different barium and strontium contents.

The different phases in the grain-boundary region appear with characteristic oxygen fine structures in the EEL spectra of Figure 5a. The O−K fine structure from BSCF corresponds to the room-temperature spectrum reported by Arnold et al.[37] and the one for the hexagonal perovskite (**A**) to the X-ray absorption near-edge structure (XANES) observed by Harvey et al.[39] Hexagonal perovskite is indicated by the absence of the Fe-$L_{2,3}$ signal, which can be seen only very weakly in Figure 5a. The oxygen fine structure of $Ba_{1-x}Sr_xCo_{2-y}Fe_yO_{5-\delta}$ (**B**) is published here for the first time. Some interesting features are noted at the Co-$L_{2,3}$ and Ba-$M_{4,5}$ edges. The Ba-M_5 white line appears constant at 788 eV for all phases and can be used as an internal standard (see Arnold et al.[38] and Efimov et al.[31]) to estimate shifts in the Co-L_3 edge. For BSCF, differences between the maxima of Ba-M_5 and Co-L_3 result in an estimate of 4.4 eV, which is smaller than the value that can be read from the spectrum reported by Efimov et al.[31] This result suggests a stronger oxidation of cobalt in BSCF in our experiment as a result of our use of high-pressure oxygen-enriched air on the feed side of the membrane. The increased oxidation of cobalt also explains why the shift of Co-L_3 to the right is only approximately 0.3 eV, compared to 0.7 eV in the experiment by Efimov et al.[31] More interesting is the observation that the Co-L_3 maximum for the hexagonal perovskite is shifted by 1.0 eV to the right as compared to BSCF. This result indicates that the oxidation state of cobalt is the highest in the hexagonal phase, which leads us directly to the reason for the phase decomposition of BSCF under the chosen operating conditions: the decomposition is induced by an unsuitable valence and spin state of cobalt, which is exposed to the strongly oxidizing conditions in the IT range and is associated with a small ionic radius that makes cobalt unstable in the cubic perovskite structure, as reported by Arnold et al.[29] and Efimov et al.[31] The temperature-dependent EELS experiment by Arnold et al.[38] also suggests a 3+ valence and low-spin state of cobalt in BSCF in the IT range. Our EELS observation (Figure 5b) of higher oxidation states of cobalt in the grain-boundary phases, as compared to BSCF, correlates

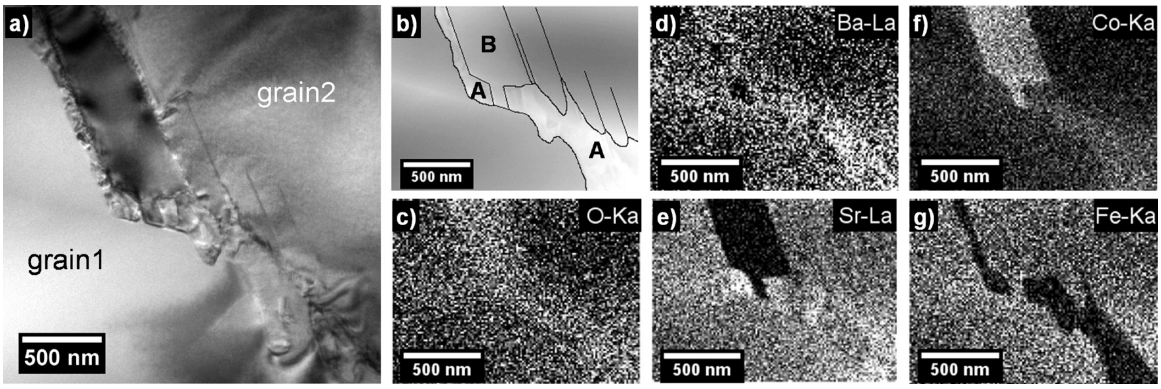

Figure 4. TEM investigation near the core/permeate side showing a grain boundary region. (a) Bright-field TEM, (b) annular dark-field STEM with grain-boundary phases labeled A and B. (c−g) EDXS elemental distributions (bright contrast correlates with high elemental concentration).

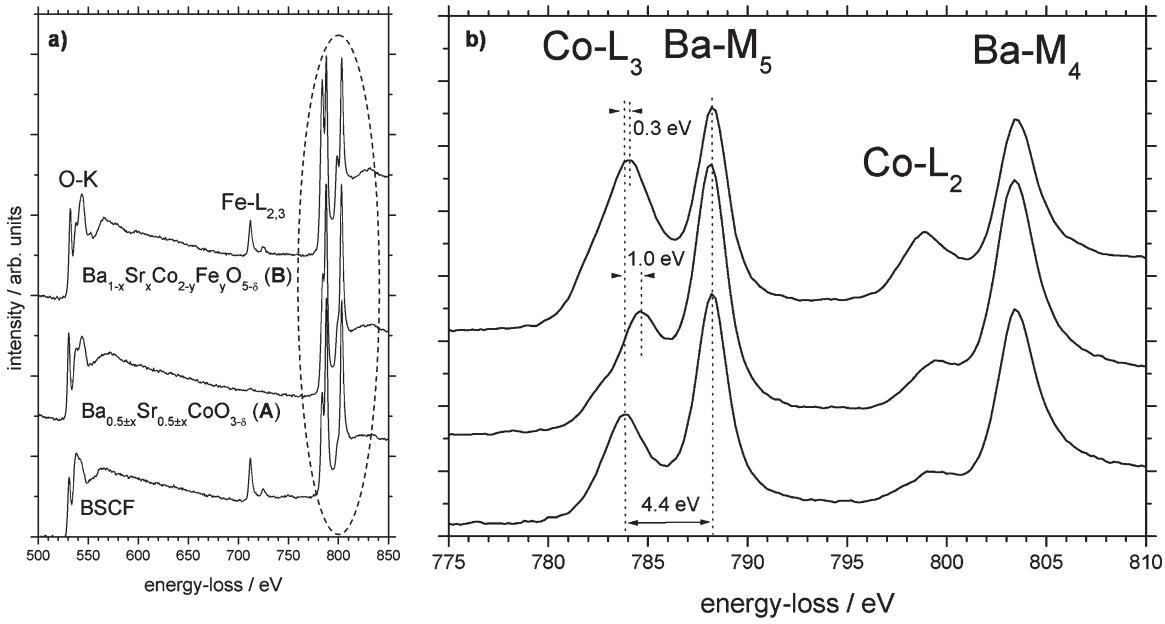

Figure 5. EEL spectra of BSCF and grain-boundary phases near the core/permeate side (see Figure 4b) showing (a) O−K, Fe-$L_{2,3}$, Co-$L_{2,3}$, and Ba-$M_{4,5}$ ionization edges; and (b) a close-up of the Co-$L_{2,3}$ and Ba-$M_{4,5}$ ionization edges.

with the higher amount of oxygen observed in the EDXS elemental distribution in Figure 4c.

Microstructure at the Shell/Feed Side. In agreement with the SEM micrographs in Figure 3, the STEM bright-field micrograph of Figure 6a shows that, near the shell/feed side, microstructure changes are not restricted to the grain boundaries. In the grain boundaries, the same phases are observed as those near the core/permeate side. However, the hexagonal phase (**A**) is the major component relative to the heavily cobalt-enriched trigonal phase (**B**), which was observed to be wrapped by phase **A**. Both phase **A** and phase **B** form extended platelets and separate grains 3 and 4 in Figure 6a. However, they are also found running straight through grain 4 almost parallel to the grain boundary. More interesting, however, are the dense arrays of hexagonal perovskite phase (**A**) that are seen in both grains, which differs from our previous observations. The circle in grain 3 marks the area from which the SAED pattern in Figure 6b was observed. The diffraction pattern shows common strong reflections from cubic BSCF and hexagonal perovskite (**A**) and additional weak reflections that are attributed only to hexagonal perovskite (**A**). The pattern was indexed in the same manner reported by Mueller et al.,[33] indicating that the close-packed layers of the cubic and hexagonal perovskite are arranged in parallel. Moreover, a comparison of Figures 6a and b indicates that the hexagonal lamellae are grown along cubic $\langle 110\rangle_c$ directions, which are denoted explicitly as $[101]_c$ and $[011]_c$ here. The cubic $\langle 110\rangle_c$ directions coincide with the average global directions of oxygen migration in cubic perovskite.[40] Therefore, the hexagonal lamellae formed in our experiments correlate with oxygen pathways in cubic BSCF. The hexagonal lamellae intergrew coherently with the cubic BSCF grains as is evident from in the HRTEM micrograph in Figure 6c. The crystals are observed in the projection along $[1\underline{1}1]_c$ such that columns of equal amounts of A-site and B-site cations are observed edge-on and appear as bright spots. Columns of oxygen are located halfway between the bright spots; however, they cannot be seen because of their weak scattering. In any event, the brightness of the spots that represent cationic columns varies locally, which suggests local compositional variations.

dx.doi.org/10.1021/cm2018086 |*Chem. Mater.* 2011, 23, 4765–4772

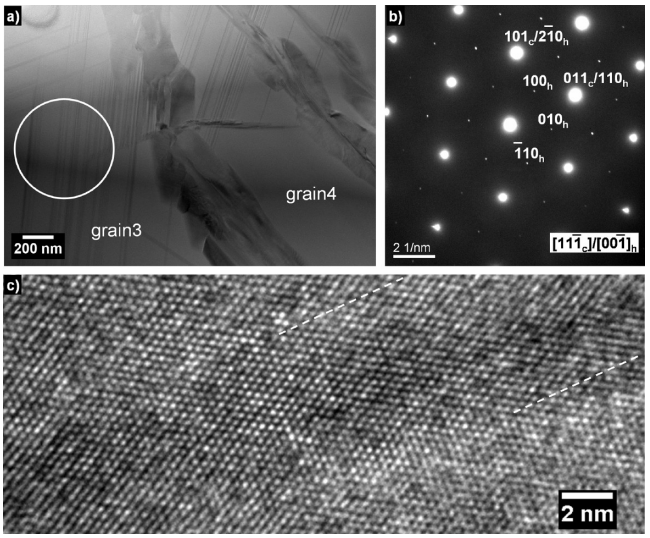

Figure 6. TEM investigation near the shell/feed side showing a grain-boundary region: (a) Bright-field STEM, (b) SAED pattern of encircled area in a, and (c) HRTEM of hexagonal lamella in cubic BSCF along [11̄1]c. Lamella is located between the dashed lines.

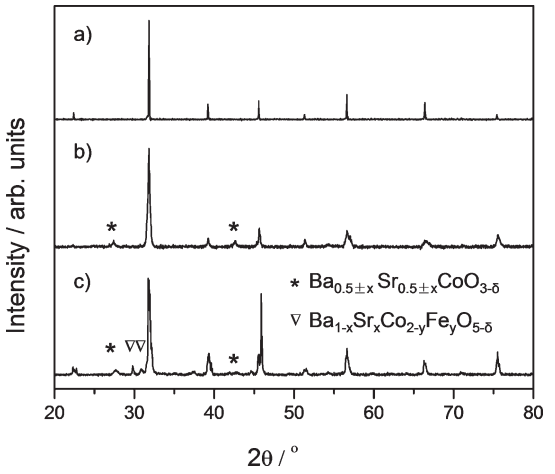

Figure 7. XRD patterns of the BSCF tube membrane: (a) shell-side surface (which is identical to the core-side surface) before permeation, (b) shell/feed-side surface, and (c) core/permeation-side surface after the long-term permeation experiment shown in Figure 2 (100 h at 950 °C, 120 h at 750 °C). For SEM micrographs, see Figure 8.

Discussion of BSCF's Partial Decomposition. With the findings concerning the local oxygen content and the cobalt valence/spin state, as previously discussed in context with Figures 4 and 5 (core/permeate side), and 6 (shell/feed side), we can identify the appearance of the hexagonal perovskite arrays with migration channels of oxygen in cubic BSCF perovskite, which exhibits the most strongly oxidizing local conditions. In addition, the evolved microstructure strongly suggests that the ideal situation of a rigid metal cationic framework has not been achieved, in that only the anionic oxygen is mobile.[41] Now, the cationic cobalt in BSCF appears to migrate to regions of higher oxygen concentration (oxygen migration pathways). There, cobalt changes its valence and spin state, and then the perovskite structure transforms. To expand the findings of Arnold et al.[29] and Efimov et al.,[31] we identify an unsuitable valence and spin state of cobalt as the main reason for the partial decomposition of BSCF while operating at 750 °C, as opposed to 950 °C. This view is supported by the observation (see Figure 3) that the microstructure changes are more severe at the oxygen-supply side (most strongly oxidizing conditions) as compared to the permeate side. Moreover, observation that the partial decomposition is restricted to the grain boundaries at the core/permeate side points out that the grain boundary environment may be significantly different from the grain volume. The preceding arguments lead then to the conclusion that, at the core/permeate side, oxygen content in the grain boundaries is higher than in the grain volume. Probably, here oxygen is transported preferentially in the grain boundary regions.

More Aspects of Evolved Microstructure. The phases identified by TEM analysis are also observed in the XRD patterns, which were collected on scans of membrane surfaces. Figure 7 shows the XRD patterns of the BSCF membrane before and after the aforementioned long-term operation. The crystal structures on both the feed and permeate sides of the starting BSCF membrane are a pure cubic-perovskite phase (Figure 3a). After the long-term operation, the cubic BSCF perovskite remains as the major phase. However, a hexagonal perovskite $Ba_{0.5\pm x}Sr_{0.5\pm x}CoO_{3-\delta}$ (**A**) has formed on the shell/feed side. Rebeilleau-Dassonneville et al.[28] and Efimov et al.[31] have observed the corresponding signals of $Ba_{0.5\pm x}Sr_{0.5\pm x}CoO_{3-\delta}$ (**A**) in XRD patterns and Efimov identified the chemical composition of this phase by STEM-EDXS as $Ba_{0.6}Sr_{0.4}CoO_{3-\delta}$. Here, however, the barium and strontium contents vary locally and the phase can be strontium-enriched (see Figure 4d and e). On the shell/feed side, the content of trigonal $Ba_{1-x}Sr_xCo_{2-y}Fe_yO_{5-\delta}$ (**B**) is too small to be detected by XRD. However, on the core/permeate side, in addition to besides $Ba_{0.5\pm x}Sr_{0.5\pm x}CoO_{3-\delta}$ (**A**), $Ba_{1-x}Sr_xCo_{2-y}Fe_yO_{5-\delta}$ (**B**) is also clearly seen as an additional phase. According to Efimov et al.,[31] trigonal $Ba_{1-x}Sr_xCo_{2-y}Fe_yO_{5-\delta}$ (**B**) can be indexed in space group $R\bar{3}m$ and is structurally related to $BaCo_{10}O_{17}$, which was reported by Sun et al.[42] Because of the structural similarity, $Ba_{1-x}Sr_xCo_{2-y}Fe_yO_{5-\delta}$ (**B**) is assumed to give an XRD pattern similar to that of $BaCo_{10}O_{17}$, even though only the structure of the latter phase has been fully resolved thus far (ICSD collection code 240501). We emphasize that the B-site (cobalt and iron) to A-site (barium and strontium) ratio we observed in our analysis is too small to match a stoichiometry of $BaCo_{10}O_{17}$. The main reflection of cubic BSCF perovskite at approximately 32° seems to be broadened. The additional intensities can be attributed to the aforementioned additional phases of hexagonal and trigonal symmetry, which evolve during the partial decomposition of the bulk cubic BSCF phase.

To sort our findings, lets have a look on Figure 8, which presents secondary-electron micrographs of the shell/feed side surface, the cross-sectional area near the shell/feed side, and the core/permeate-side surface of the BSCF membrane before and after the oxygen-permeation experiment of Figure 2 (100 h at 950 °C and 120 h at 750 °C). After the long-term oxygen-permeation experiment in the IT range, secondary phases protrude from the bulk grains at the surface of the shell/feed side (see Figure 8d). In the corresponding broken cross-section (Figure 8e), an approximately 1 μm thick grain-boundary phase is clearly observed. According to the XRD results (see Figure 7b) and the aforementioned TEM results (Figure 6), the secondary phase is primarily the hexagonal perovskite $Ba_{0.5\pm x}Sr_{0.5\pm x}CoO_{3-\delta}$ (**A**). At the core/permeate side (Figure 8f), decoration of grain boundaries is clearly visible, the decorations are composed of trigonal $Ba_{1-x}Sr_xCo_{2-y}Fe_yO_{5-\delta}$ (**B**) and hexagonal perovskite $Ba_{0.5\pm x}Sr_{0.5\pm x}CoO_{3-\delta}$ (**A**), as was analyzed in

dx.doi.org/10.1021/cm2018086 |Chem. Mater. 2011, 23, 4765–4772

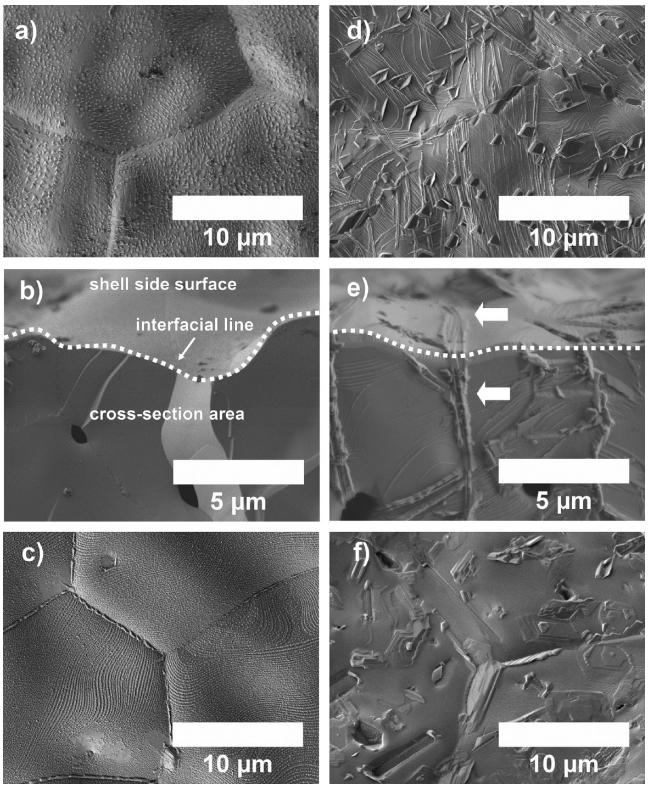

Figure 8. Microstructures of the BSCF perovskite tube membrane before and after the oxygen permeation experiment: Surface view of shell/feed side (a) before and (d) after permeation; broken cross-sectional area near the shell/feed side (b) before and (e) after permeation; surface view of the core/permeation side (c) before and (f) after permeation. For the permeation experiment, see Figure 2; for the XRD patterns, see Figure 7c. White arrows in e mark secondary phase at grain boundary.

context with Figure 4. In the vicinity of internal porosity, hexagonal features (**A**) also appear inside the grains.

CONCLUSIONS

The long-term phase stability and oxygen permeability of dead-end BSCF tube membranes (400 mm long, 10 mm outer diameter, 1 mm wall thickness) were studied under practice-relevant permeation conditions at 950 and 750 °C. A high oxygen purity of almost 100 vol. % and a stable oxygen-permeation flux were observed during the long-term operation for 100 h at 950 °C. However at 750 °C, the oxygen-permeation flux continuously decreases with time, and the BSCF tube membrane is structurally unstable. The phase instability of BSCF is due to a partial decomposition of the bulk cubic perovskite phase into a hexagonal perovskite, $Ba_{0.5\pm x}Sr_{0.5\pm x}CoO_{3-\delta}$, and a trigonal mixed oxide $Ba_{1-x}Sr_xCo_{2-y}Fe_yO_{5-\delta}$. At the core/permeate side, the formation of secondary phases is predominantly restricted to the grain boundaries. At the shell/feed side, which constitutes the region of highest oxygen chemical potential during dynamic oxygen flux through the BSCF membrane material, the formation of secondary phases is most pronounced. Here, the secondary phase is mainly the cobalt-enriched hexagonal perovskite, which is not only found in grain boundaries, but also runs through the bulk grains, leading to important internal stresses, that give rise to membrane cracking at the oxygen-feed side. The stronger formation of secondary phases at higher local oxygen chemical potentials during dynamic oxygen flux suggests that the valence and spin state of the most flexible redoxable cation (i.e., cobalt) is the key to an understanding of BSCF's decomposition in the intermediate temperature range. The phase stability of BSCF (i.e., the proper redox states of cobalt) can be maintained by operating BSCF membranes in the high-temperature regime (950 °C).

AUTHOR INFORMATION

Corresponding Author

*E-mail: armin.feldhoff@pci.uni-hannover.de.

ACKNOWLEDGMENT

The EU is thanked for financing in the 7th Framework Program the IP Innovative Catalytic Technologies & Materials for the Next Gas to Liquid Processes (NEXT-GTL). The State of Lower Saxony is thanked for financing in frame of a bottom-up project to found the Niedersächsisch Technische Hochschule (NTH). G. Centi, Messina, and G. Iaquaniello, Rome, are thanked for their stimulating discussions. The authors appreciate Professor H. H. Wang in Guangzhou for fruitful discussions. The authors thank Dr. R. Kriegel from the Fraunhofer Institute for Ceramic Technologies and Systems (IKTS) for making the BSCF tube and for his helpful remarks.

REFERENCES

(1) Bose, A. C., *Inorganic Membranes for Energy and Environmental Applications*; Springer: New York, 2009; p 4.
(2) Lide, D. R. *CRC Handbook of Chemistry and Physics*; CRC Press: Boca Raton, FL, 1997.
(3) Armstrong, P. A.; Bennet, D. L.; Fprster, E. P. T.; van Stein, E. E. ITM Oxygen for Gasification. In *2004 Gasification Technology Conference: New Technologies Development*; Washington, D.C., Oct 3−6, 2004; Gasification Technologies Council: Arlington, VA, 2004.
(4) Bouwmeester, H. J. M. *Catal. Today* **2003**, *82*, 141.
(5) Tsai, C. Y.; Dixon, A. G.; Moser, W. R.; Ma, Y. H. *AIChE J.* **1997**, *43*, 2741.
(6) Shao, Z. P.; Dong, H.; Xiong, G. X.; Gong, Y.; Yang, W. S. *J. Membr. Sci.* **2001**, *183*, 181.
(7) Yang, W. S.; Wang, H. H.; Zhu, X. F.; Lin, L. W. *Top. Catal.* **2005**, *35*, 155.
(8) Caro, J.; Caspary, K. J.; Hamel, C.; Hoting, B.; Kolsch, P.; Langanke, B.; Nassauer, K.; Schiestel, T.; Schmidt, A.; Schomacker, R.; Seidel-Morgenstern, A.; Tsotsas, E.; Voigt, I.; Wang, H. H.; Warsitz, R.; Werth, S.; Wolf, A. *Ind. Eng. Chem. Res.* **2007**, *46*, 2286.
(9) Jiang, H. Q.; Cao, Z. W.; Schirrmeister, S.; Schiestel, T.; Caro, J. *Angew Chem Int Ed.* **2010**, *49*, 5656.
(10) Jiang, H. Q.; Liang, F. Y.; Czuprat, O.; Efimov, K.; Feldhoff, A.; Schirrmeister, S.; Schiestel, T.; Wang, H. H.; Caro, J. *Chem.—Eur. J.* **2010**, *16*, 7898.
(11) Jiang, H. Q.; Wang, H. H.; Werth, S.; Schiestel, T.; Caro, J. *Angew. Chem., Int. Ed.* **2008**, *47*, 9341.
(12) Jiang, H. Q.; Wang, H. H.; Liang, F. Y.; Werth, S.; Schiestel, T.; Caro, J. *Angew. Chem., Int. Ed.* **2009**, *48*, 2983.
(13) Jiang, H. Q.; Xing, L.; Czuprat, O.; Wang, H. H.; Schirrmeister, S.; Schiestel, T.; Caro, J. *Chem. Commun.* **2009**, 6738.
(14) Wang, H. H.; Kolsch, P.; Schiestel, T.; Tablet, C.; Werth, S.; Caro, J. *J. Membr. Sci.* **2006**, *284*, 5.
(15) Liang, F. Y.; Jiang, H. Q.; Schiestel, T.; Caro, J. *Ind. Eng. Chem. Res.* **2010**, *49*, 9377.
(16) Tan, X. Y.; Wang, Z. G.; Meng, B.; Meng, X. X.; Li, K. *J. Membr. Sci.* **2010**, *352*, 189.
(17) Ito, W.; Nagai, T.; Sakon, T. *Solid State Ionics* **2007**, *178*, 809.

(18) Zhu, X. F.; Sun, S. M.; Cong, Y.; Yang, W. S. *J. Membr. Sci.* **2009**, *345*, 47.
(19) Teraoka, Y.; Zhang, H. M.; Furukawa, S.; Yamazoe, N. *Chem. Lett.* **1985**, 1743.
(20) Yang, L.; Wu, Z. T.; Jin, W. Q.; Xu, N. P. *Ind. Eng. Chem. Res.* **2004**, *43*, 2747.
(21) Luo, H. X.; Tian, B. B.; Wei, Y. Y.; Wang, H. H.; Jiang, H. Q.; Caro, J. *AIChE J.* **2010**, *56*, 604.
(22) Martynczuk, J.; Liang, F. Y.; Arnold, M.; Sepelak, V.; Feldhoff, A. *Chem. Mater.* **2009**, *21*, 1586.
(23) Efimov, K.; Halfer, T.; Kuhn, A.; Heitjans, P.; Caro, J.; Feldhoff, A. *Chem. Mater.* **2010**, *22*, 1540.
(24) Shao, Z. P.; Yang, W. S.; Cong, Y.; Dong, H.; Tong, J. H.; Xiong, G. X. *J. Membr. Sci.* **2000**, *172*, 177.
(25) Shao, Z. P.; Haile, S. M. *Nature* **2004**, *431*, 170.
(26) Kriegel, R.; Kircheisen, R.; Töpfer, J. *Solid State Ionics* **2010**, *181*, 64.
(27) van Veen, A. C.; Rebeilleau, M.; Farrusseng, D.; Mirodatos, C. *Chem. Commun.* **2003**, 32.
(28) Rebeilleau-Dassonneville, M.; Rosini, S.; van Veen, A. C.; Farrusseng, D.; Mirodatos, C. *Catal. Today* **2005**, *104*, 131.
(29) Arnold, M.; Gesing, T. M.; Martynczuk, J.; Feldhoff, A. *Chem. Mater.* **2008**, *20*, 5851.
(30) Švarcová, S.; Wiik, K.; Tolchard, J.; Bouwmeester, H. J. M.; Grande, T. *Solid State Ionics* **2008**, *178*, 1787.
(31) Efimov, K.; Xu, Q. A.; Feldhoff, A. *Chem. Mater.* **2010**, *22*, 5866.
(32) Arnold, M.; Wang, H.; Martynczuk, J.; Feldhoff, A. *J. Am. Ceram. Soc.* **2007**, *90*, 3651.
(33) Mueller, D. N.; De Souza, R. A.; Weirich, T. E.; Roehrens, D.; Mayer, J.; Martin, M. *Phys. Chem. Chem. Phys.* **2010**, *12*, 10320.
(34) Kriegel, R.; Kircheisen, R. DE 10 2009 050 019 B3, 2011.03.17, 2009.
(35) Tong, J.; Yang, W.; Cai, R.; Zhu, B.; Lin, L. *Catal. Lett.* **2002**, *78*, 129.
(36) Spillman, R. Economics of Gas Separation Membrane Processes. In *Membrane Science and Technology*; Noble, R. D., Stern, S. A., Eds.; Elsevier: New York, 1996; Vol. 2, p 269.
(37) Wang, H. H.; Werth, S.; Schiestel, T.; Caro, J. *Angew. Chem., Int. Ed.* **2005**, *44*, 6906.
(38) Arnold, M.; Xu, Q.; Tichelaar, F. D.; Feldhoff, A. *Chem. Mater.* **2009**, *21*, 635.
(39) Harvey, A. S.; Yang, Z.; Infortuna, A.; Beckel, D.; Purton, J. A.; Gauckler, L. J. *J. Phys.: Condens. Matter* **2009**, *21*, 015801.
(40) Yashima, M., Structural disorder, diffusion pathway of mobile oxide ions, and crystal structure in perovskite-type oxides and related materials. In *Perovskite Oxide for Fuel Cells*, Ishihara, T., Ed.; Springer: Dordrecht, The Netherlands, 2009; p 117.
(41) Goodenough, J. B., Crystalline solid electrolytes II: Materials design. In *Solid State Electrochemistry*; Bruce, P. G., Ed.; Cambridge University Press: Cambridge, U.K., 1995; p 43.
(42) Sun, J. L.; Yang, M.; Li, G. B.; Yang, T.; Liao, F. H.; Wang, Y. X.; Xiong, M.; Lin, J. H. *Inorg. Chem.* **2006**, *45*, 9151.